IJMMM International Journal of Minerals, Metallurgy and Materials 矿物冶金与材料学报（英文版）

Numerical simulation of microwave-induced cracking and melting of granite based on mineral microscopic models

Xiaoli Su, Diyuan Li, Junjie Zhao, Mimi Wang, Xing Su, and Aohui Zhou

Cite this article as:
Xiaoli Su, Diyuan Li, Junjie Zhao, Mimi Wang, Xing Su, and Aohui Zhou, Numerical simulation of microwave-induced cracking and melting of granite based on mineral microscopic models, *Int. J. Miner. Metall. Mater.*, 31(2024), No. 7, pp. 1512-1524. https://doi.org/10.1007/s12613-023-2821-4

View the article online at SpringerLink or IJMMM Webpage.

Articles you may be interested in

Subhnit K. Roy, Deepak Nayak, Nilima Dash, Nikhil Dhawan, and Swagat S. Rath, Microwave-assisted reduction roasting–magnetic separation studies of two mineralogically different low-grade iron ores, *Int. J. Miner. Metall. Mater.*, 27(2020), No. 11, pp. 1449-1461. https://doi.org/10.1007/s12613-020-1992-5

Shuang Huang, Hua-lan Xu, Sheng-liang Zhong, and Lei Wang, Microwave hydrothermal synthesis and characterization of rare-earth stannate nanoparticles, *Int. J. Miner. Metall. Mater.*, 24(2017), No. 7, pp. 794-803. https://doi.org/10.1007/s12613-017-1463-9

Zhi-yuan Ma, Yong Liu, Ji-kui Zhou, Mu-dan Liu, and Zhen-zhen Liu, Recovery of vanadium and molybdenum from spent petrochemical catalyst by microwave-assisted leaching, *Int. J. Miner. Metall. Mater.*, 26(2019), No. 1, pp. 33-40. https://doi.org/10.1007/s12613-019-1707-y

Yang He, Jian Liu, Jian-hua Liu, Chun-lin Chen, and Chang-lin Zhuang, Carbothermal reduction characteristics of oxidized Mn ore through conventional heating and microwave heating, *Int. J. Miner. Metall. Mater.*, 28(2021), No. 2, pp. 221-230. https://doi.org/10.1007/s12613-020-2037-9

Hamed Gholami, Bahram Rezai, Ahmad Hassanzadeh, Akbar Mehdilo, and Mohammadreza Yarahmadi, Effect of microwave pretreatment on grinding and flotation kinetics of copper complex ore, *Int. J. Miner. Metall. Mater.*, 28(2021), No. 12, pp. 1887-1897. https://doi.org/10.1007/s12613-020-2106-0

Peng Liu, Li-bo Zhang, Bing-guo Liu, Guang-jun He, Jin-hui Peng, and Meng-yang Huang, Determination of dielectric properties of titanium carbide fabricated by microwave synthesis with Ti-bearing blast furnace slag, *Int. J. Miner. Metall. Mater.*, 28(2021), No. 1, pp. 88-97. https://doi.org/10.1007/s12613-020-1985-4

IJMMM WeChat

QQ author group

INTERNATIONAL JOURNAL OF
Minerals, Metallurgy and Materials

Volume 31, Number 7, July 2024
Page 1512

Research Article https://doi.org/10.1007/s12613-023-2821-4

Numerical simulation of microwave-induced cracking and melting of granite based on mineral microscopic models

Xiaoli Su, Diyuan Li✉, Junjie Zhao, Mimi Wang, Xing Su, and Aohui Zhou

School of Resources and Safety Engineering, Central South University, Changsha 410083, China

(Received: 29 July 2023; revised: 22 December 2023; accepted: 27 December 2023)

Abstract: This study introduces a coupled electromagnetic–thermal–mechanical model to reveal the mechanisms of microcracking and mineral melting of polymineralic rocks under microwave radiation. Experimental tests validate the rationality of the proposed model. Embedding microscopic mineral sections into the granite model for simulation shows that uneven temperature gradients create distinct molten, porous, and nonmolten zones on the fracture surface. Moreover, the varying thermal expansion coefficients and Young's moduli among the minerals induce significant thermal stress at the mineral boundaries. Quartz and biotite with higher thermal expansion coefficients are subjected to compression, whereas plagioclase with smaller coefficients experiences tensile stress. In the molten zone, quartz undergoes transgranular cracking due to the α–β phase transition. The local high temperatures also induce melting phase transitions in biotite and feldspar. This numerical study provides new insights into the distribution of thermal stress and mineral phase changes in rocks under microwave irradiation.

Keywords: microwave; numerical modeling; microcracking; phase change; granite

1. Introduction

With the continuous development of deep mining, the effectiveness and environment-friendly characteristics of excavation operations in the deep underground are increasingly in demand [1–3]. Microwave heating has emerged as a potential solution in underground mining operations, assisting in deep drilling [4–6], hard rock breaking [7–10], and grinding [11–12]. Currently, two primary approaches are used for microwave-assisted rock fragmentation. The first approach uses microwave energy to melt rocks [4,13]. The second approach uses microwaves to weaken the rocks before employing mechanical tools, such as tunnel boring and drilling machines, for excavation [9,14–16]. Rocks are composed of minerals, which vary considerably in their microwave absorption ability, thermal properties, and mechanical characteristics [17]. This diversity poses challenges in understanding the mechanisms of microwave-induced melting or fracturing in rocks, thereby hindering potential industrial applications.

To gain a deeper understanding of the mechanisms underlying the effects of microwave heating on rock mass fragmentation, previous studies assessed the microwave absorption capabilities of many individual minerals. Chen *et al*. [18] investigated 40 types of minerals and found that most metal sulfides can be easily heated. Lu *et al*. [19] conducted a microwave treatment on 11 rock-forming minerals and observed that most of them had weak microwave absorption capabilities. Furthermore, Zheng *et al*. [20] highlighted the role of iron content in enhancing the microwave absorption of minerals. Although the microwave absorption capabilities of individual minerals are known, the interaction of microwaves with polymineralic rocks is still not well studied. Microwaves heterogeneously heat the constituent minerals, resulting in thermal gradients and subsequent microcracks within the rock [13,21]. Consequently, the presence of strong absorbers, the varied composition and properties of the minerals are both key factors in the formation of intergranular and transgranular cracks during microwave heating [22]. However, observing thermal gradients and identifying microcracking within polymineralic rocks during microwave heating in laboratory experiments is challenging. The reason for this is the limitations of current measurement instruments in capturing internal temperature and specimen deformation details.

Numerical simulations offer valuable insights into the interaction between microwave radiation and polymineralic rocks or minerals [23–25]. For intact rocks, most numerical studies have focused on macrofracturing in heterogeneous rocks and microwave-induced damage to rock mass strength [26–28]. For minerals, some modeling approaches are often restricted to single or dual mineral simulations to reduce the computational complexity caused by heterogeneity. For example, Zheng and Sun [29] conducted electromagnetic simu-

---

✉ Corresponding author: Diyuan Li E-mail: diyuan.li@csu.edu.cn

lations to determine the electric field strengths of individual minerals. Cui *et al*. [30] provided a micromodel of two-mineral stacks and examined the thermal stress generated between minerals with contrasting thermomechanical characteristics. Li *et al*. [31] investigated the microscale stress–strain variability in pegmatite using a digitized thin section. Their findings revealed that the highest von Mises stress was along the quartz–plagioclase interface. The above-mentioned literature provides valuable insights into the numerical modeling of the effects of microwave radiation and rocks or minerals. However, the thermal response of the microscopic mineral assemblages within the rock has not been well studied. The mechanism of mineral assemblage cracking and melting behavior under microwave radiation is unclear and needs to be further explored.

To fill these gaps, this study aims to develop a model that incorporates microscopic mineral assemblages in a rock specimen. For this purpose, microwave heating experiments were initially conducted on granite specimens to gather data on temperature rise, cracking, and melting characteristics. The resulting cracked specimens were then analyzed using scanning electron microscopy and energy-dispersive X-ray spectroscopy (SEM-EDX) to examine their microscopic characteristics and obtain actual mineral assemblages. Based on the obtained microscopic mineral assemblage, a comprehensive electromagnetic–thermal–mechanical numerical model was developed and validated. Finally, a series of numerical simulations were performed to investigate the thermal response and evolution of thermal stress within and between minerals.

2. Experimental

2.1. Sample preparation

The granite tested in this study was obtained from Quanzhou City, Fujian Province. Fig. 1 illustrates the type and content of minerals in the granite, as determined using a polarizing microscope. The primary minerals in the granite slice are plagioclase (Pl), K-feldspar (K), quartz (Q), hornblende (Hbl), and biotite (Bt). The granite exhibits a fine-grained structure, with particle sizes in the range 0.05–0.5 mm. For basic mechanical testing and microwave heating experiments, cylindrical specimens, each with a diameter of 50 mm and a height of 100 mm, were prepared. Table 1 details the basic physical and mechanical properties of granite, including its density (2770 kg/m³), Young's modulus (44.7 GPa), and Poisson's ratio (0.22).

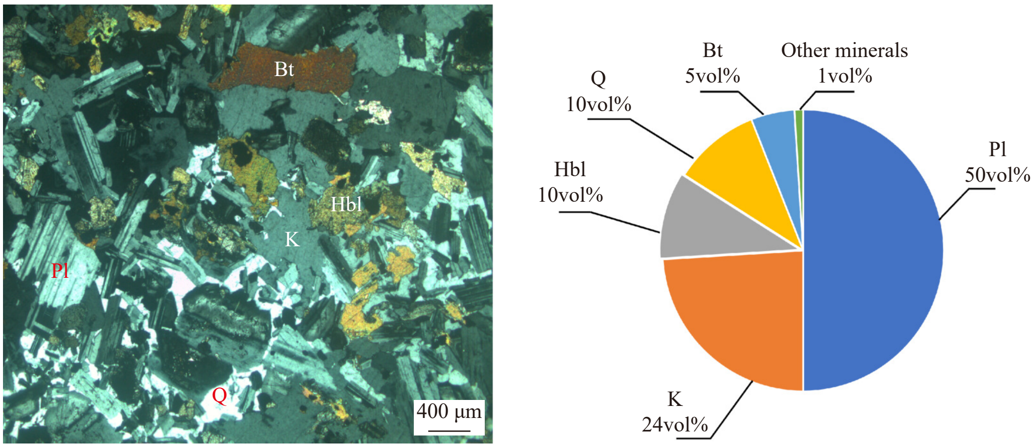

(a) Mineral distribution

(b) Mineral content

Fig. 1. (a) Optical microscopy image and (b) mineral content.

Table 1. Physical and mechanical properties of tested granite

Density / (g·cm^{-3})	Uniaxial compressive strength / MPa	Young's modulus / GPa	Poisson's ratio
2.77	203.36	44.70	0.22

2.2. Experimental procedure

To minimize the effect of moisture, a cylindrical granite specimen was initially dried in an oven at 105°C for 48 h. Subsequently, the specimen was heated using a multimode microwave oven at a frequency of 2.45 GHz (Fig. 2). This oven comprises a circular cavity, a noncontact infrared thermometer, and four microwave sources, each delivering up to 2 kW of power. The specimen was placed on an 8 cm-high mullite pad beneath the waveguide ports (Fig. 2). The samples were heated at a power of 5.4 kW for 400 s, during which the temperature at the center of each sample was monitored using an infrared thermometer. After heating, the oven door was opened, and the sample was allowed to cool to room temperature for subsequent observation, including SEM-EDX analysis.

2.3. Results of the microwave heating experiment

Fig. 3 illustrates the temperature–exposure time relationship at the top of the granite specimen. Notably, the initial phase (0–100 s) marks the period of increasing irradiation

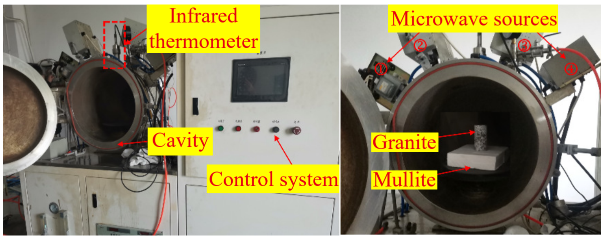

Fig. 2. Microwave heating system.

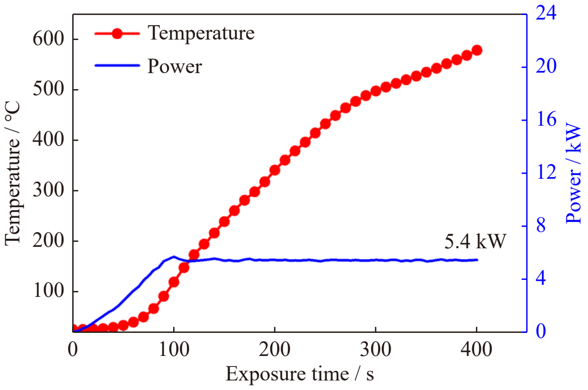

Fig. 3. Temperature evolution of granite specimens with exposure time under microwave treatment.

power, gradually adjusting to reach the target of 5.4 kW. Currently, the surface temperature of the granite reaches approximately 118.6°C. Following the phase from 100 to 280 s, the temperature exhibits a linear increase with the extended exposure time. However, beyond 280 s, the temperature curve shows a notable deviation due to the onset of cracking and melting in the granite. Finally, the peak temperature is up to 582.5°C at 400 s.

Fig. 4(a) shows images of the fracture characteristics of granite following microwave heating. On the surface of the specimen, a circumferential crack appears in the upper part of the granite, almost separating the specimen into two halves. Additionally, an axial crack extends from the middle to the upper part of the specimen. At the intersection of these axial and circumferential cracks, the presence of black melt material is noted. This observation leads to the conclusion that granite breakage is primarily due to mineral melting and macrocracks induced by high temperatures. Fig. 4(b) further illustrates the presence of molten, porous, and nonmolten zones on the fracture surface.

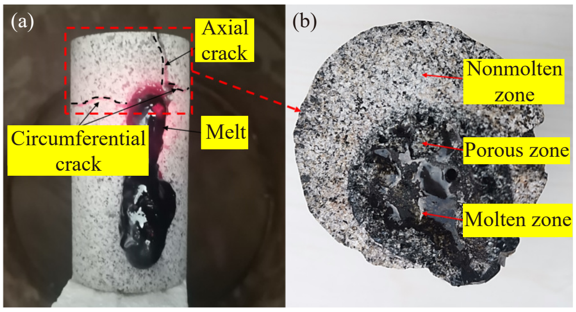

Fig. 4. Fracture and molten images of granite after microwave irradiation: (a) thermal fracture and molten substance on the specimen surface and (b) molten, porous, and nonmolten zones on the fracture surface.

3. Microstructural analysis and numerical model construction

This section aims to identify the micromorphology and mineral composition of molten, porous, and nonmolten zones, ultimately intending to construct an accurate microscopic mineral model. Initially, SEM-EDX is employed to observe these specific zones. The microscopic data thus obtained are then used to develop the model in COMSOL.

3.1. Microstructural analysis of the microwave-heated granite

3.1.1. Mineral morphology identification

As illustrated in Fig. 5(a), the entire fracture section of the granite underwent electron microscopy after gold spraying. During this analysis, three characteristic points were selected to observe the microstructures across various zones of the granite fracture surface. The SEM images in Fig. 5(b1)–(b3) reveal that the molten zone surface appears smooth and glossy; however, some scratches are visible at 50× magnification. These scratches may be caused by the movement of the molten material or external wear during the cooling or sampling process.

In the porous zone (Fig. 5(c1)–(c3)), debris, pores, and pits are evident. Under microwave heating, gas generation occurs within the specimen. However, because of the low porosity of the granite specimen, gas diffusion is limited, leading to the gradual formation of microbubbles in the melt. As the temperature and steam pressure inside the specimen increase, the rock debris breaks away, forming pits [32]. Thus, it is difficult to identify mineral boundaries that are covered by flowing melt in the melting and porous zones. In contrast, as shown in Fig. 5(d1)–(d3), multiple intergranular and transgranular cracks are distributed in the nonmolten zone. In this zone, the matrix maintains clear mineral boundaries and shapes.

3.1.2. Mineral composition identification

Polarizing microscopic observations reveal that granite primarily comprises plagioclase, quartz, K-feldspar, biotite, and hornblende. The chemical compositions of these minerals are $(Ca,Na)_{2-3}(Mg,Fe,Al)_5(Si,Al)_8O_{22}(OH,F)_2$, $K(Mg,Fe)_3AlSi_3O_{10}(F,OH)_2$, $KAlSi_3O_8$, SiO_2, and $NaAlSi_3O_8CaAl_2Si_2O_8$, respectively. The EDX imaging technique is used to observe the distribution of chemical elements, which assists in identifying the mineral composition. For instance, Fig. 6(a) shows that chemical elements such as Si (31.78wt%), O (38.58wt%), Al (15.22wt%), K (6.13wt%), Na (3.36wt%), and Fe (3.17wt%) are uniformly distributed in the molten zone. This indicates that quartz is the dominant mineral in this zone, followed next by smaller quantities of feldspar and biotite. As the internal temperature of granite increases, quartz, feldspar, and biotite melt, flow, and concentrate, eventually breaking through and flowing along the fracture surface. Similarly, the porous zone of the granite mainly consists of quartz and K-feldspar (Fig. 6(b)).

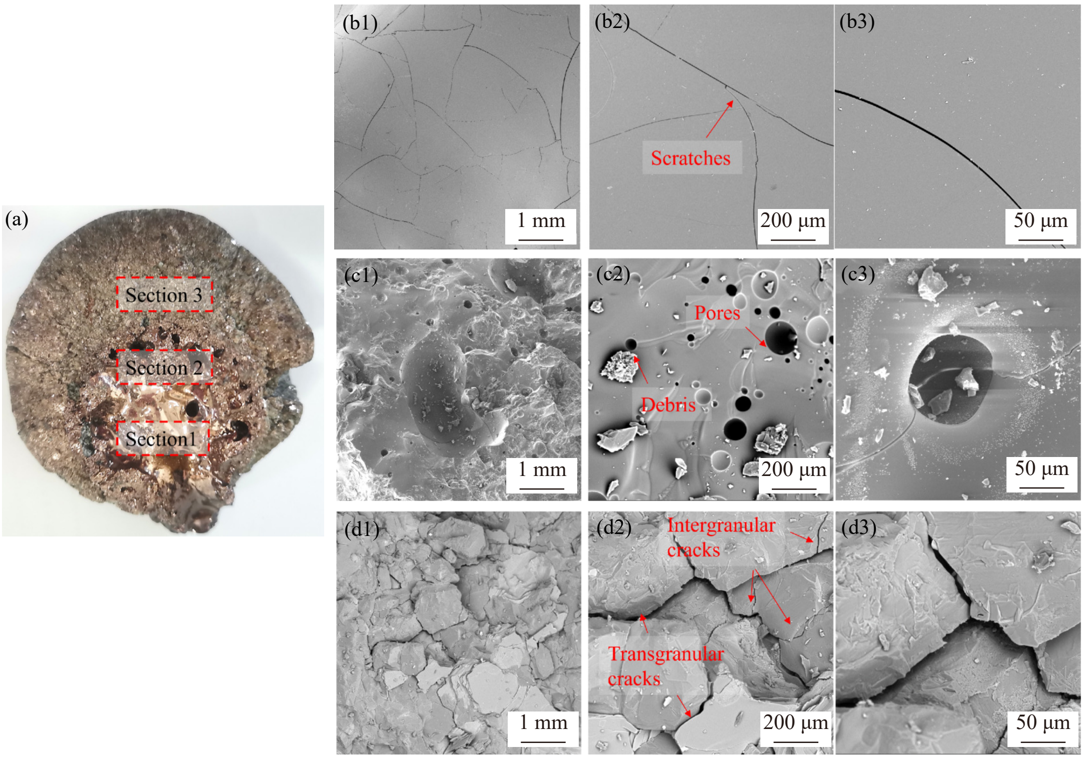

Fig. 5. Scanning electron microscopy (SEM) images of granite after microwave irradiation: (a) schematic diagram of observation points; (b1–b3) molten zone (Section 1); (c1–c3) porous zone (Section 2); (d1–d3) non-molten zone (Section 3).

Fig. 6(c) shows notable differences in the content and distribution of elements between the nonmolten zone and other zones. In the EDX maps, biotite and hornblende can be distinguished from other minerals based on their iron (Fe) distribution. Additionally, the overlapping areas of potassium (K) and iron (Fe) suggest biotite, while the overlapping areas of sodium (Na) and calcium (Ca) indicate the presence of plagioclase. The EDX diagram shows that in addition to the obvious intergranular cracks between various minerals, partial transgranular cracks also exist inside quartz and plagioclase, and layer separation phenomena occur in some layered biotite minerals.

3.2. Geometric modeling of the numerical model

3.2.1. Geometric model construction

To accurately model the mineral microstructure, the following steps were taken:

(1) Image processing with imageJ: As illustrated in Fig. 7(a), the SEM-EDX images were first subjected to grayscale correction and denoising to enhance their quality. Edge detection was then applied to these images to extract mineral boundaries and generate vector images with discrete geometries.

(2) Mineral assignment: each mineral in the thin sections was identified based on the SEM-EDX image, and specific parameters were assigned to them as listed in Table 2. The molten and porous sections mainly consisted of quartz, biotite, and feldspar. However, obtaining accurate mineral morphology was challenging because the molten material obscured the mineral boundaries. Therefore, the same SEM images were used for various sections. We assumed that K-feldspar replaced the corresponding position of hornblende (Fig. 7(b)).

(3) Modeling with AutoCAD: as shown in Fig. 7(c), the vector image depicting the mineral boundaries was imported into AutoCAD. Within AutoCAD, the vector image was transformed into rectangular thin sections, each measuring 1.30 mm in length, 1.30 mm in width, and 0.1 mm in thickness. Three such sections representing the melting, porous, and nonmelting zones were then incorporated into the granite model. The dimensions of the microwave oven and the specimen in the model were also made consistent with those used in the experiment.

(4) Simulation with COMSOL software: The entire geometric model was imported into COMSOL multiphysics for microwave heating simulation. In this simulation, specific assumptions and boundary conditions were set to simplify the model: 1) All materials, including granite and minerals, were considered to be continuous and isotropic. 2) Rectangular ports were excited by transverse electromagnetic waves, and port boundary conditions were applied at the entrance of the waveguide (Fig. 7(d)). 3) The cavity walls and waveguide walls were perfect conductors, with any heat and deformation occurring only in the granite region. 4) Impedance boundary conditions were set for the cavity walls, insulation conditions for the granite surface, and a mechanical boundary condition at the bottom of the specimen.

(5) Grid Partitioning: As depicted in Fig. 8, a grid generation method was established to ensure the convergence and accuracy of the model, considering the significant size differences between the mineral sections, specimens, and microwave ovens. For micromineral sections, a free triangular

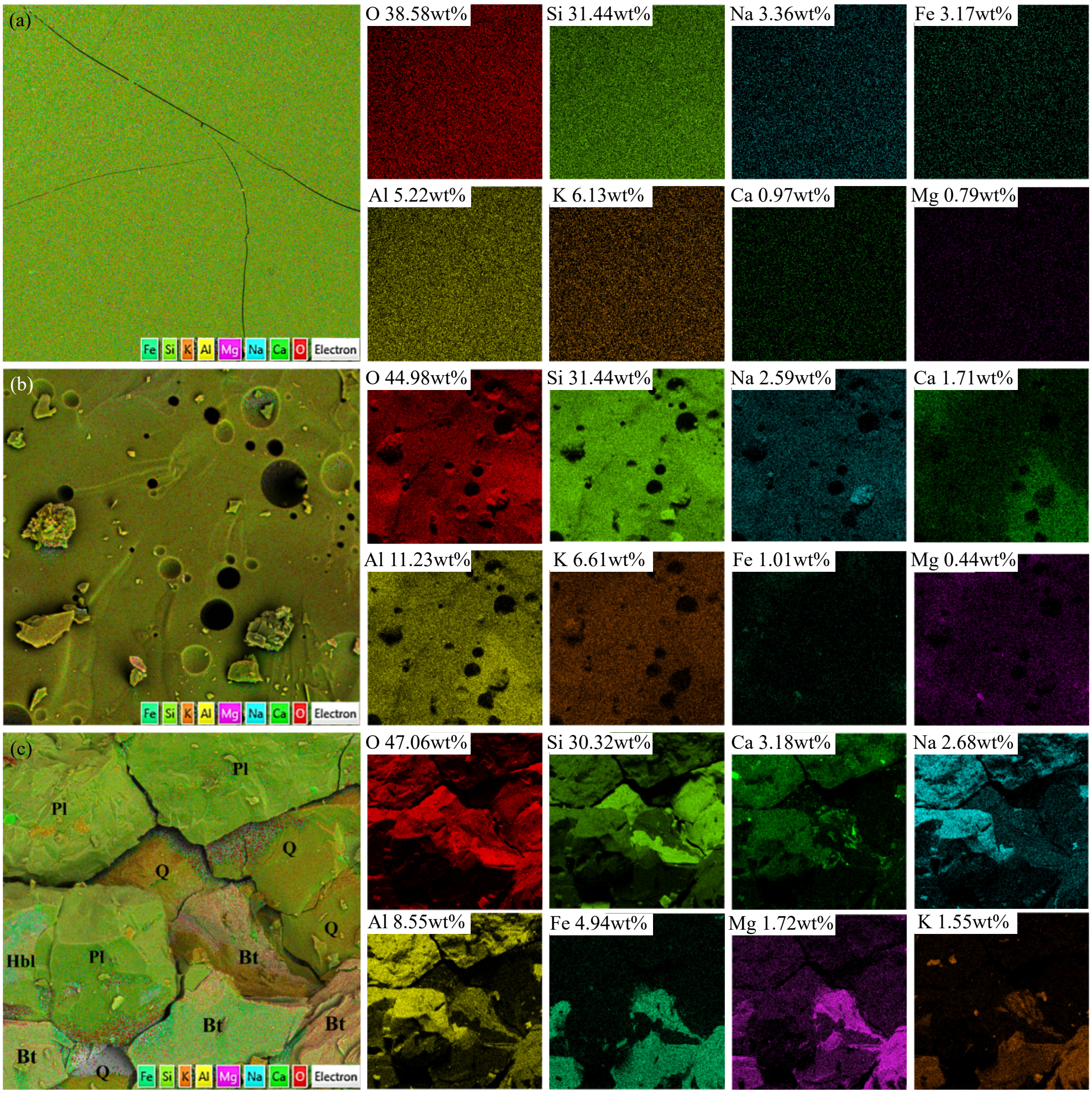

Fig. 6. EDX images of the granite specimen: (a) molten zone; (b) porous zone; (c) nonmolten zone.

mesh was created along the mineral surface, with a minimum mesh unit size of 0.025 mm. Subsequently, a sweeping mesh was applied to the mineral sections along their thickness (Fig. 8(c)). For the oven and granite specimens, a free tetrahedral grid was used, with a maximum unit size of <0.2 times the wavelength. The resulting mesh quality after segmentation was 0.66, ensuring the reliability of the model.

3.2.2. Governing equations

The mathematical representation for the coupled electromagnetic–thermal–mechanical process of rock during microwave radiation is as follows:

(1) Electromagnetic excitation.

The electromagnetic field in a microwave cavity is described by Maxwell's equations [24]:

$$\nabla\times\mu_{\rm r}^{-1}(\nabla\times\boldsymbol{E})-k_0^2\left(\varepsilon_{\rm r}-\frac{{\rm j}\sigma}{\omega\varepsilon_0}\right)\boldsymbol{E}=0 \tag{1}$$

$$\varepsilon_{\rm r}=\varepsilon'-{\rm j}\varepsilon'' \tag{2}$$

$$\omega=2\pi f \tag{3}$$

where $\mu_{\rm r}$ and $\varepsilon_{\rm r}$ are the relative permeability and permittivity of the specimen, respectively. $\varepsilon_{\rm r}$ can be determined by the dielectric constant ε' and dielectric loss factor ε''. ε_0 and k_0 are the permittivity and wave velocity of the free space, respectively. $\boldsymbol{E}$ is the electric field intensity, σ is the conductivity, and ω is the angular frequency. j is $\sqrt{-1}$, and f is the input frequency.

After granite is applied to electromagnetic waves, a portion of the electromagnetic energy is converted into heat because of its dielectric loss [23].

$$Q_{\rm e}=\frac{1}{2}{\rm Re}(\boldsymbol{J}\cdot\boldsymbol{E}+{\rm j}\omega\boldsymbol{B}\cdot\boldsymbol{H}) \tag{4}$$

where $Q_{\rm e}$ represents the electromagnetic power loss; Re denotes the real part of the relative primitively of materials; and $\boldsymbol{J}$, $\boldsymbol{B}$, and $\boldsymbol{H}$ are the current density, magnetic flux density, and magnetic field intensity, respectively.

(2) Thermal transfer and phase change.

Transient heat transfer equations can describe the temperature distribution in the specimen, with the heat source provided by the electromagnetic field loss [23] as follows:

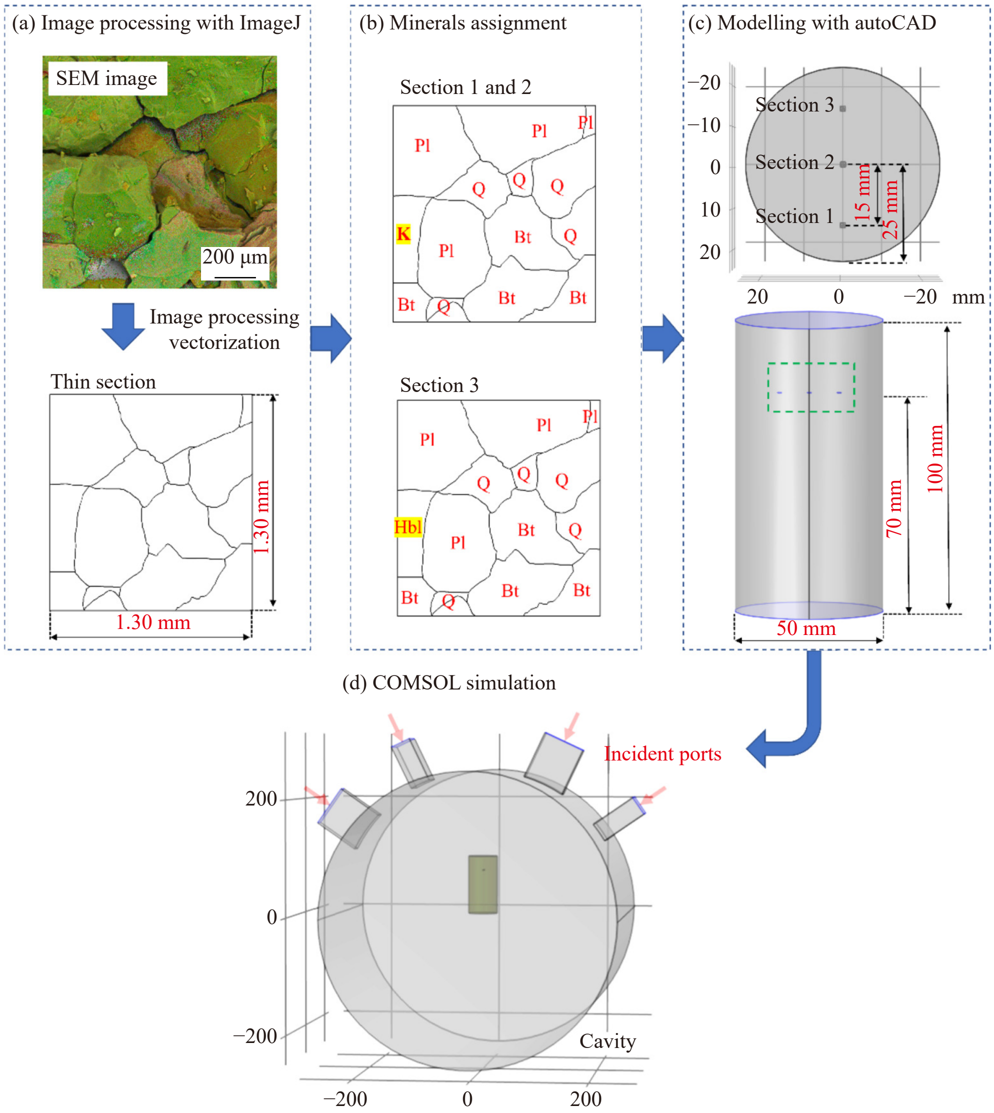

Fig. 7. **Processes of building the geometric model.**

Table 2. **Material properties in the model were obtained from the literature [20,22,28–29,31,33]**

Material	Volume ratio / %	Relative permeability	Dielectric constant	Loss factor	Specific heat capacity / $(J\cdot kg^{-1}\cdot K^{-1})$	Heat conductivity / $(W\cdot m^{-1}\cdot K^{-1})$	Thermal expansion coefficient / $(10^{-6}\ K^{-1})$	Poisson's ratio	Young's modulus / GPa	Density / $(g\cdot cm^{-3})$
Plagioclase	50	1.00	6.07	0.039	650.0	2.00	3.70	0.35	70.0	2.63
K-feldspar	24	1.00	5.61	0.118	730.0	2.34	7.50	0.29	60.0	2.62
Quartz	10	1.00	4.72	0.014	731.0	4.94	12.10	0.17	80.0	2.65
Hornblende	10	1.00	14.45	0.324	710.0	2.85	6.50	0.15	61.6	3.24
Biotite	5	1.00	7.48	0.456	770.0	3.14	12.10	0.20	20.0	3.05
Granite		1.00	6.67	0.104	682.8	2.50	6.12	0.22	44.7	2.77

Note: In addition to Poisson's ratio, density, and elastic modulus, the thermophysical parameters and dielectric constant of granite are all calculated from the volume percentage of the main minerals in Fig. 1(b) [31].

$$\rho C_{\mathrm{p}} \frac{\partial T}{\partial t} + \rho C_{\mathrm{p}} \boldsymbol{u}_{\mathrm{trans}} \cdot \nabla T + \nabla \cdot (k \nabla T) = Q_{\mathrm{e}} + Q_{\mathrm{ted}} \tag{5}$$

where C_{p}, ρ, and k are the specific heat capacity, mass density, and thermal conductivity of the specimen, respectively. $\boldsymbol{u}_{\mathrm{trans}}$ denotes the velocity vector of translational motion, and Q_{ted} is the thermoelastic damping. T and t are temperature and time, respectively.

At high temperatures, some minerals undergo phase changes, such as the α–β phase transition of quartz and the melting phase change of biotite and feldspar. The properties of the phase change materials can be specified according to the apparent heat capacity formula [34]:

$$C_{\mathrm{p,eff}} = \theta_1 C_{\mathrm{p},1} + \theta_2 C_{\mathrm{p},2} + L_{1\to 2}\, \partial \left(\frac{1}{2} \frac{\theta_2 - \theta_1}{\theta_1 + \theta_2} \right) / \partial T \tag{6}$$

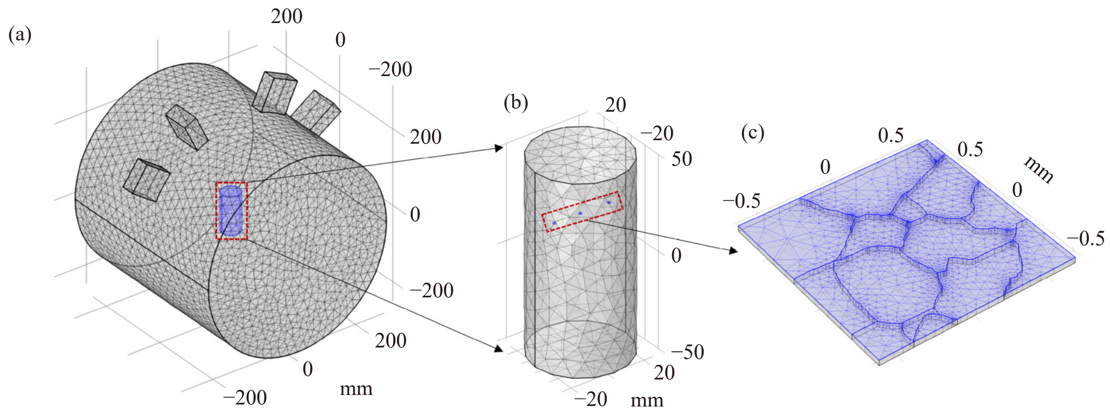

Fig. 8. Grid partitioning method: (a) mesh division of the furnace; (b) mesh division of the specimen; (c) mesh division of thin sections.

$$k_{\text{eff}} = \theta_1 k_1 + \theta_2 k_2 \tag{7}$$

$$\theta_1 + \theta_2 = 1 \tag{8}$$

where $C_{\text{p,eff}}$, $C_{\text{p,1}}$, and $C_{\text{p,2}}$ are the specific heat capacities of minerals before and after the phase change, respectively. Similarly, k_{eff} is the effective thermal conductivity. Besides, k_1, k_2, θ_1, and θ_2 are the thermal conductivity and volume fraction of the mineral before and after the phase transition, respectively; $L_{1\to2}$ is the latent heat of the phase change.

(3) Thermal expansion.

The thermally induced strain due to temperature changes within the material is assumed to be the result of isotropic expansion and is given by [31]:

$$\varepsilon_T = \alpha (T - T_{\text{ref}}) \tag{9}$$

where ε_T is the thermal strain, α is the coefficient of thermal expansion, and T_{ref} is the strain reference temperature.

4. Numerical simulation results

4.1. Simulation of temperature distribution

4.1.1. Temperature distribution within rock

In Fig. 9, simulation results are compared with the experimental data obtained from the infrared thermometer gun. The power adjustment period is not considered during the simulation; therefore, the initial temperature is set at 118.6°C. The graph indicates that the simulated temperature in the top center of the specimen closely corresponds with experimental data.

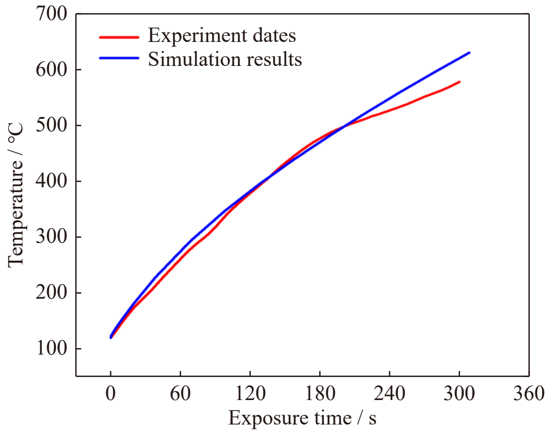

Fig. 9. Comparison of the temperature simulation results with the experimental data.

Fig. 10 compares the photo of granite and a snapshot of the numerical simulation results after 300 s of 5.4 kW microwave radiation. The simulation results indicate that temperatures exceeding 1000°C are concentrated in the center of the granite specimen, which is the primary reason for its melting. Meanwhile, significant temperature differences within the specimen can induce macrocracks. In Fig. 10(b), the area of high-temperature concentration on the simulated fracture surface is consistent with the melting area on the fracture surface. These observations are critical for comprehending the melting position of granite when subjected to microwave heating, as well as the mechanism behind macro-

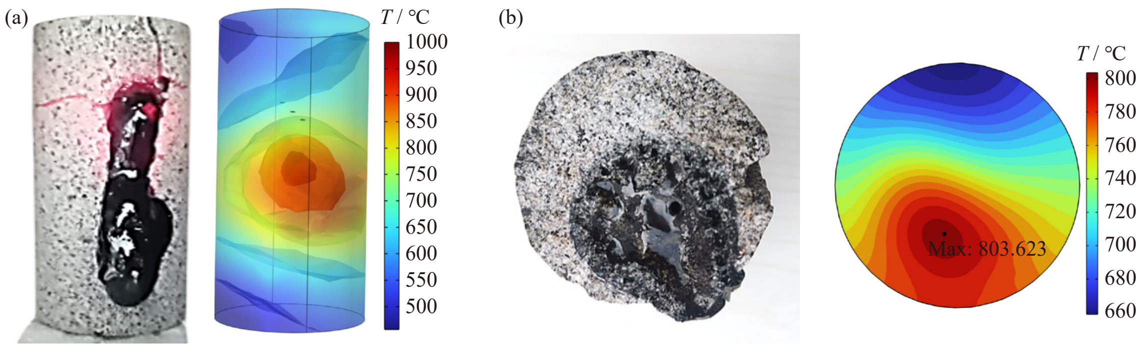

Fig. 10. Experiment photos and temperature field simulation of granite after 300 s of microwave radiation: (a) granite surface; (b) fracture surface.

scopic crack formation in granite.

4.1.2. Temperature distribution on mineral sections

To enhance the understanding of the thermal characteristics of the granite sample, Table 3 displays the temperature distribution across each section during various heating durations (0, 100, and 300 s). Initially, the biotite temperature is notably higher than that of other minerals, which can be attributed to its superior dielectric properties. Both the melting zone (Section 1) and the porous zone (Section 2) exhibit a similar temperature distribution because of their similar mineral compositions. In the nonmolten zone (Section 3), in addition to biotite, the presence of hornblende also contributes to a high-temperature concentration because of its high loss coefficient.

Table 3. Temperature distribution in thin sections after 300 s of microwave radiation

Time / s	Molten zone	Porous zone	Nonmolten zone
0	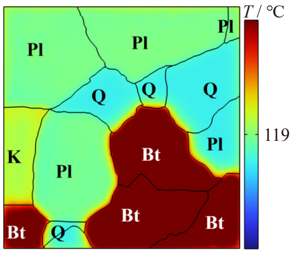	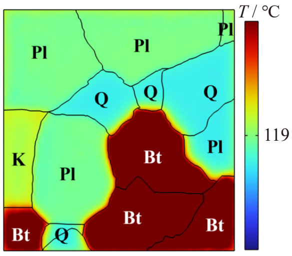	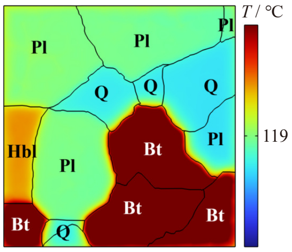
100	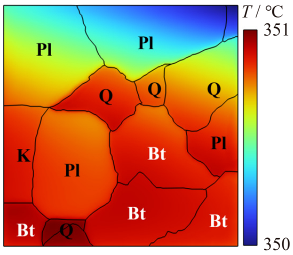	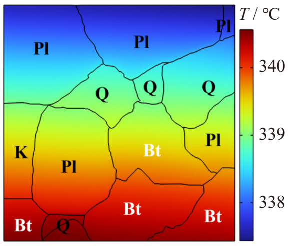	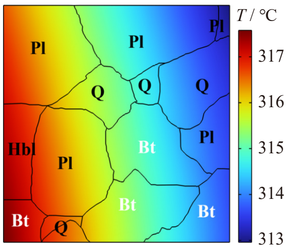
300	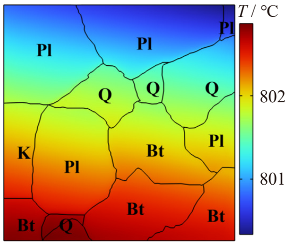	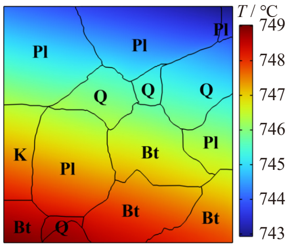	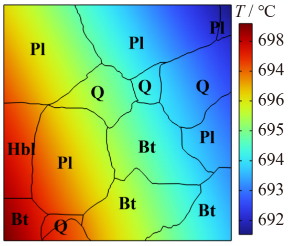

As microwave radiation exposure time increases, the temperature profile evolves, which is influenced by the thermal conductivities of each mineral and electromagnetic field distribution. In the melting zone, the high thermal conductivity of quartz leads to the highest temperature. Eventually, a peak temperature of 802°C is reached within the quartz at 300 s. Because of spatial differences, the porous zone maintains a lower temperature than the melting zone. In the nonmelting zone, the temperature distribution is unique. Influenced by the temperature gradient in the surrounding area of the section (Table 3), the high temperature is predominantly concentrated on the lower left side rather than on the quartz.

4.2. Simulation of the thermal stress

The microwave heating experiment was followed by SEM imaging, which revealed a high number of transgranular and intergranular cracks in the unmolten section. To gain insight into the crack initiation mechanism, the stress distribution within the microscopic mineral sections was calculated.

4.2.1. Von Mises stress in minerals sections

The von Mises stress, a scalar that considers the effects of all stress components, can be used to analyze the stress distribution in microscopic minerals. As depicted in Fig. 11, the von Mises stress distribution in Section 3 is uneven after 300 s of microwave irradiation. Quartz exhibits the highest stress values, followed by plagioclase, biotite, and hornblende, according to the Mises stress distribution on the *A*-*A*′, *B*-*B*′, and *C*-*C*′ lines. Notably, the stress value between quartz and plagioclase reached up to 340 MPa, indicating significant stress at the mineral boundaries (Fig. 11(d)).

Fig. 12 presents a comparison of the von Mises stress distribution in the nonmelting, porous, and melting zones after 300 s of microwave heating. In the porous and melting zones, minerals experience higher von Mises stress due to increased temperature distribution after heating. Compared with plagioclase, K-feldspar is subjected to higher von Mises stress because of its high coefficient of thermal expansion. Additionally, the stress significantly increases at the boundaries between minerals.

4.2.2. Thermal stress in minerals

To differentiate the stress types in each mineral, Fig. 13 shows the stress component σ_{xx} of the nonmmolten zone (Section 3) after 300 s of microwave radiation. Quartz and biotite are mainly subjected to compressive stress, while pla-

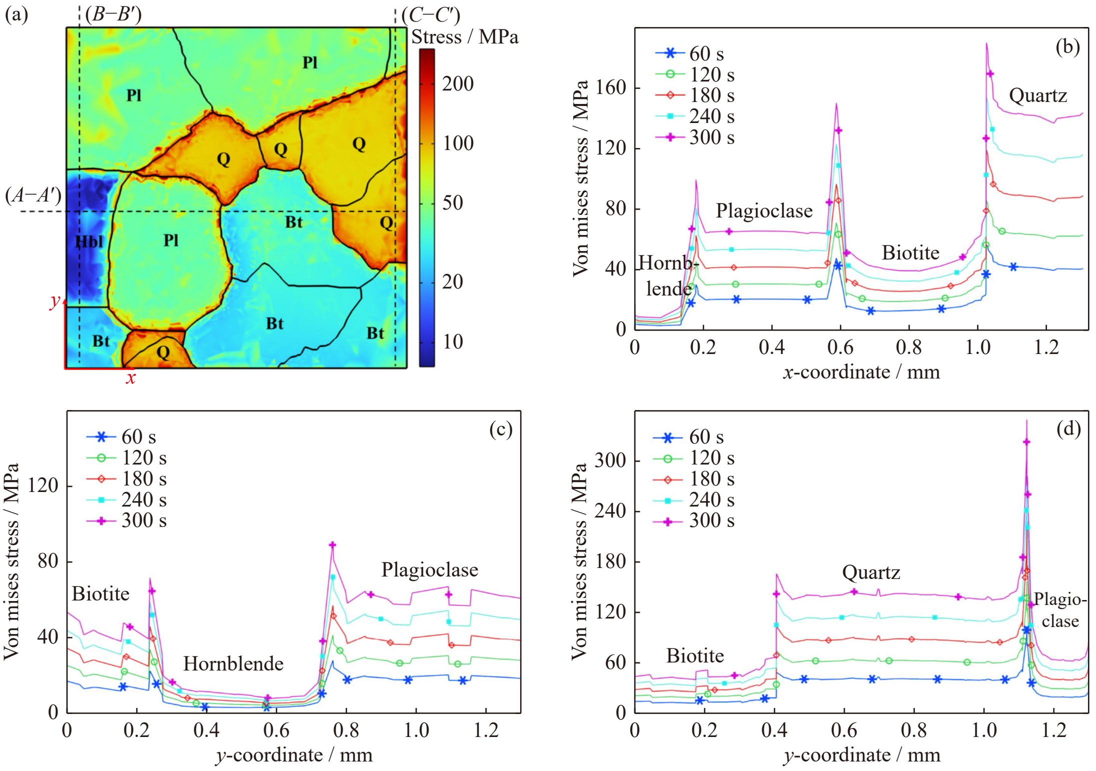

Fig. 11. Von Mises stress distribution: (a) Mises stress distribution in the nonmolten zone (Section 3) after 300 s of microwave heating; (b) Mises stress distribution along *A–A′*; (c) Mises stress distribution along *B–B′*; (d) Mises stress distribution along *C–C′*.

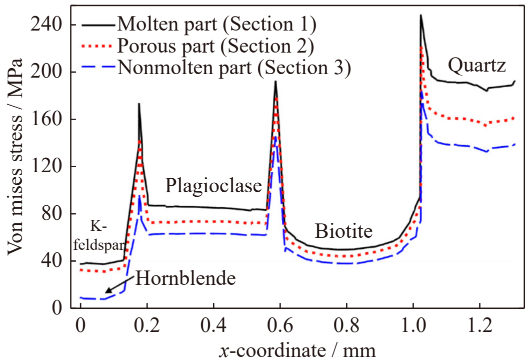

Fig. 12. Von Moses stress distributions along the *A–A′* line in various zones after 300 s of microwave radiation.

gioclase and hornblende mainly experience tensile stress.

As Fig. 13(b) illustrates, quartz undergoes a compressive stress of 130 MPa. Because of its larger coefficient of thermal expansion and higher elastic modulus, quartz is more prone to thermal expansion when subjected to microwave heating. However, this expansion is constrained by adjacent minerals, resulting in maximum compressive stress. Biotite, which also possesses a significant coefficient of thermal expansion, experiences compression from neighboring minerals. In contrast to quartz, biotite possesses a lower elastic modulus, indicating a reduced capacity for deformation. As a result, biotite experiences less compression under similar conditions. After 300 s of heating, plagioclase with a lower thermal expansion coefficient is subjected to a tensile stress of 60 MPa, which exceeds its tensile strength and causes transgranular cracks. Hornblende undergoes only small tensile stress because the surrounding plagioclase and biotite exert negligible reactive forces on it. Considering the behavior observed in these minerals, it is evident that thermal stress plays a critical role in their microstructural integrity. When the thermal

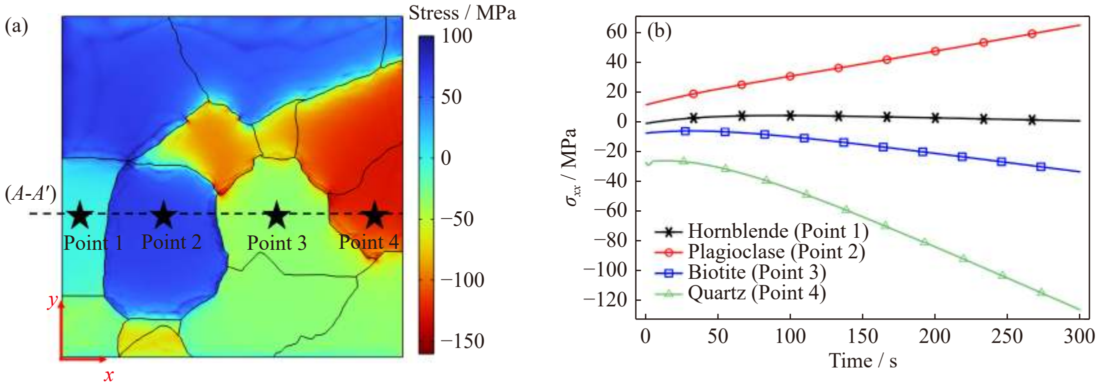

Fig. 13. Stress distribution in the nonmolten zone: (a) σ_{xx} distribution in Section 3; (b) σ_{xx} distribution in the minerals.

stress exceeds the tensile strength of minerals such as plagioclase and hornblende, transgranular cracks can occur.

Fig. 14 demonstrates that in the melting zone, quartz, K-feldspar, and biotite are subjected to compressive thermal stress whereas plagioclase is subjected to tensile stress. Because of the higher temperatures in the molten zone, the tensile thermal stress in plagioclase reaches 80 MPa, which is significantly higher than the tensile strength of plagioclase. Therefore, plagioclase in the melting zone is more prone to tensile failure, resulting in transgranular cracks.

4.2.3. Thermal stress in mineral boundaries

Fig. 11 shows the significant Mises stress distribution along mineral boundaries, where thermal stress is the primary cause of intergranular cracks. Because of the uneven shapes and physical properties of the minerals, stress distribution at the boundaries is more complex. Illustrating this, Fig. 15(a) displays the principal stress lines along the boundary of the unmelted section. The stress perpendicular to the boundaries between quartz and other minerals is mainly a negative third principal stress, indicating compression at these boundaries. In contrast, the stress perpendicular to the boundaries between plagioclase and other minerals is mainly the first principal stress, which has a positive direction and represents tensile stress at the boundaries. Meanwhile, the principal stress perpendicular to the boundaries of hornblende and biotite is also a negative third principal stress, although its magnitude is significantly smaller than that at the quartz boundary.

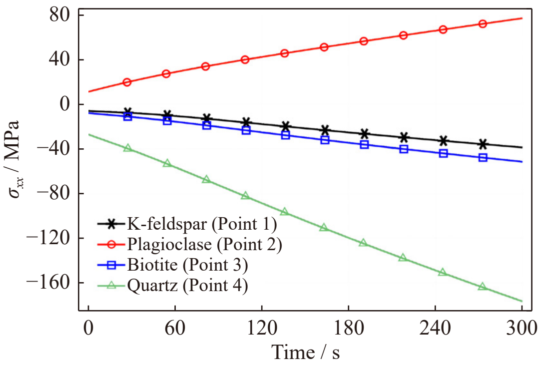

Fig. 14. Variations in σ_{xx} of minerals in the molten zone with the heating time.

After 300 s of microwave radiation, tensile stresses of 98, 156, and 161 MPa are generated at the boundaries between plagioclase and hornblende, plagioclase and quartz,and plagioclase and biotite, respectively. When the boundary stress surpasses the bond strength between minerals, tensile intergranular cracks may form around plagioclase, as depicted in Fig. 15(b). Notably, significant compressive stress is observed around quartz, with the quartz–plagioclase boundary experiencing the highest compressive stress. This is attributed to the much higher thermal expansion coefficient of quartz than that of plagioclase. Additionally, despite the similarity in expansion coefficients between biotite and quartz, the difference in elastic moduli of biotite and quartz can lead to compressive stress near 160 MPa at their interface.

4.3. Simulation of mineral phase changes

Quartz is a mineral known for its extraordinary hardness, high compressive strength, and resistance to penetration. However, when exposed to high temperatures, the α–β phase transformation of quartz can lead to the generation of transgranular cracks [7,35]. Fig. 16(a) illustrates the phase transition process of quartz in the molten, porous, and nonmolten zones. In the melting zone, the temperature within quartz reaches the α–β quartz transition point (573°C) as the radiation time increases, changing the volume fraction of α-quartz from 1 to 0. Subsequently, the porous zone also reaches the phase transition temperature at approximately 220 s. In nonmolten areas, α-quartz transforms into β-quartz at 250 s, resulting in transgranular cracks.

According to the SEM-EDX results shown in Fig. 6(a) and (b), the melted material predominantly consists of molten biotite, quartz, and feldspar. In the numerical simulation that employs the phase change equation, the melting process of biotite is observed. As depicted in Fig. 16(b), biotite undergoes a melting phase transition only in the molten and porous zones. When subjected to a microwave field, biotite

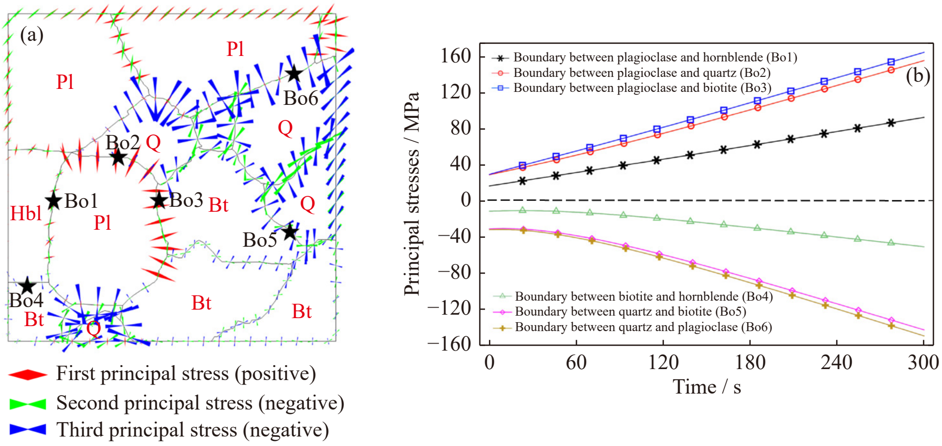

Fig. 15. Distribution of principal stress on the boundary of minerals in the nonmolten zone (Section 3): (a) Principal stress distribution in the boundary after 300 s of microwave heating; (b) variations in the principal stress value at mineralogical boundaries with the heating time.

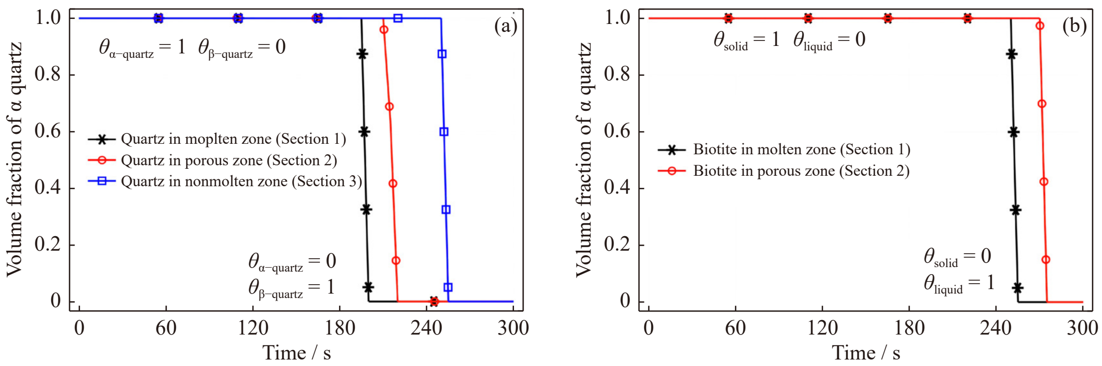

Fig. 16. Phase change of quartz and biotite in various zones: (a) α–β quartz transition in various zones with the heating time; (b) melting phase change of biotite in the molten and porous zones (solid-liquid phase transition of biotite).

heats up to 700°C [36], transitioning from a solid to a liquid state. This finding highlights the importance of considering the melting point of biotite in microwave mineral treatment processes to avoid excessive melting.

Under standard atmospheric pressure, plagioclase with a high albite content starts to melt at 850°C [37], and K-feldspar and quartz require over 1200°C to melt [36]. However, the numerical model shows a maximum temperature of only 802°C in the melting zone, which is below the melting threshold for plagioclase. This discrepancy is mainly due to the model not accounting for water evaporation. Both capillary water and hydrated minerals are strong microwave absorbers. When exposed to microwave radiation, capillary water rapidly heats up and transfers heat to adjacent minerals. Consequently, the local temperature inside the specimen likely reaches 850°C, which is sufficient to melt some plagioclase. Moreover, water evaporation in the granite specimen rapidly increases the vapor pressure [32,38], which lowers the melting temperatures of quartz and feldspar [34–35] and facilitates their melting [39–40]. Under these conditions, the melting temperature of plagioclase can even fall below 800°C [36], leading to the melting phase transformation of some feldspars.

5. Discussion

The modeling approach adopted in this study innovatively embedded microscopic mineral sections into granite before performing the electromagnetic–thermal–mechanical coupled simulations. To make the model more convincing, the cavity dimensions of the microwave oven and the positions of the embedded micromineral sections were closely matched to those in the laboratory experiments. This allowed for direct observation of the temperature and thermal stress distribution within the microscopic mineral sections under microwave heating.

Compared with laboratory experiments, numerical simulations revealed temperature gradients within the specimen. These simulations also showed temperature variations across microscopic mineral sections in various locations that traditional sensors could not detect. Furthermore, this study explored the melting process of granite specimens in microwaves by simulating the mineral phase transitions. The microscopic mineral sections in the high-temperature zone experienced the earliest biotite phase transition. This phenomenon was consistent with the melting observed in the laboratory. Therefore, the strategy of positioning mineral sections in varied locations not only demonstrated the selective heating characteristic of microwaves but also aided in pinpointing where melting will occur inside the specimen. Although high-power microwave equipment can heat rocks to a molten state, its substantial energy consumption cannot be ignored. In applications of microwave-assisted rock fragmentation or grinding where complete melting of rocks is undesirable [6,36,41], this model can effectively predict the onset and location of melting. Consequently, this model aids in optimizing microwave parameters to minimize energy consumption.

Unlike previous studies on single minerals or two-mineral combinations [20], this research approach more comprehensively revealed the fracture mechanisms within microscopic mineral combinations under microwave heating. The findings of this study suggest that differences in mineral thermal expansion coefficients predominantly cause thermal stress at mineral boundaries, such as those between quartz and plagioclase and between plagioclase and biotite [31,35]. Meanwhile, the difference in the Young’s modulus of minerals is also the reason for the high thermal stress at the boundary, such as those between quartz and biotite. However, previous studies have rarely emphasized this factor. The reason for the formation of intergranular cracks in plagioclase is that it underwent the highest tensile stress. In quartz, the combination of high thermal stress and the α–β phase transformation led to the formation of intergranular cracks. The method proposed in this study not only demonstrated the complex fracture mechanism of micromineral combinations under microwave action but also provided a powerful modeling method for future research. This method can be applied to various types of polymineralic rocks to further explore and verify the effects of microwave heating.

However, based on our current model, the limitations of finite element methods in accurately describing the fracture of microcracks make it difficult to visualize the fracture process of thermal cracks. Future research efforts will focus on integrating damage factors or applying phase-field fracture methods to improve fracture visualization in mineral sections. These advancements are expected to provide further insights into transgranular and intergranular fractures.

6. Conclusions

The temperature distribution and cracking mechanism of granite under microwave radiation were investigated through experimental tests and numerical simulations. The main conclusions are as follows:

(1) Both the experiments and simulations showed that granite samples heated in a 5.4 kW multimode cavity for 300 s reached nearly 600°C at the surface center. Selective heating of microwaves caused high local temperatures inside the granite, leading to cracking and melting.

(2) In the mineral sections, significant von Mises stresses were noted on the surfaces and boundaries of quartz, primarily due to its higher thermal expansion and elastic modulus. Under microwave conditions, quartz and biotite exhibit significant thermal expansion, resulting in considerable compressive stress.

(3) Integrating SEM-EDX analysis with numerical simulations revealed that plagioclase and its boundaries were prone to developing intergranular and transgranular cracks when subjected to tensile forces.

(4) By embedding microscopic mineral sections, quartz is observed underwent α–β phase transitions, resulting in transgranular cracks. In the molten and porous zones, biotite experienced melting phase transitions.

Acknowledgements

The work was financially supported by the National Natural Science Foundation of China (No. 52074349) and the Graduate Research Innovation Project of Hunan Province, China (No. CX20230194).

Conflict of Interest

All authors declare that they have no financial interests or personal relationships that could have appeared to influence the work reported in this paper.

References

[1] K.Z. Xia, C.X. Chen, X.T. Liu, X.M. Liu, J.H. Yuan, and S. Dang, Assessing the stability of high-level pillars in deeply-buried metal mines stabilized using cemented backfill, *Int. J. Rock Mech. Min. Sci.*, 170(2023), art. No. 105489.

[2] K.Z. Xia, C.X. Chen, T.L. Wang, Y. Zheng, and Y. Wang, Estimating the geological strength index and disturbance factor in the Hoek–Brown criterion using the acoustic wave velocity in the rock mass, *Eng. Geol.*, 306(2022), art. No. 106745.

[3] X.Q. He, C. Zhou, D.Z. Song, *et al.*, Mechanism and monitoring and early warning technology for rockburst in coal mines, *Int. J. Miner. Metall. Mater.*, 28(2021), No. 7, p. 1097.

[4] E. Jerby, V. Dikhtyar, O. Aktushev, and U. Grosglick, The microwave drill, *Science*, 298(2002), No. 5593, p. 587.

[5] D. P. Lindroth, W. R. Berglund, R. Morrell, and J. R. Blair, Microwave assisted drilling in hard rock, *Tunnels Tunnelling Int.*, 25(1993), No. 6, p. 24.

[6] M.Z. Gao, B.G. Yang, J. Xie, *et al.*, The mechanism of microwave rock breaking and its potential application to rock-breaking technology in drilling, *Pet. Sci.*, 19(2022), No. 3, p. 1110.

[7] P. Hartlieb, M. Toifl, F. Kuchar, R. Meisels, and T. Antretter, Thermo-physical properties of selected hard rocks and their relation to microwave-assisted comminution, *Miner. Eng.*, 91(2016), p. 34.

[8] Y.L. Zheng and L. He, TBM tunneling in extremely hard and abrasive rocks: Problems, solutions and assisting methods, *J. Cent. South Univ.*, 28(2021), No. 2, p. 454.

[9] X.T. Feng, J.Y. Zhang, C.X. Yang, *et al.*,, A novel true triaxial test system for microwave-induced fracturing of hard rocks, *J. Rock Mech. Geotech. Eng.*, 13(2021), No. 5, p. 961.

[10] X.T. Feng, S.P. Li, C.X. Yang, *et al.*, The influence of the rotary speed of a microwave applicator on hard-rock fracturing effect, *Rock Mech. Rock Eng.*, 55(2022), No. 11, p. 6963.

[11] W. Wei, Z.S. Shao, Y.Y. Zhang, R.J. Qiao, and J.P. Gao, Fundamentals and applications of microwave energy in rock and concrete processing–A review, *Appl. Therm. Eng.*, 157(2019), art. No. 113751.

[12] H. Gholami, B. Rezai, A. Hassanzadeh, A. Mehdilo, and M. Yarahmadi, Effect of microwave pretreatment on grinding and flotation kinetics of copper complex ore, *Int. J. Miner. Metall. Mater.*, 28(2021), No. 12, p. 1887.

[13] T. Peinsitt, F. Kuchar, P. Hartlieb, *et al.*, Microwave heating of dry and water saturated basalt, granite and sandstone, *Int. J. Min. Miner. Eng.*, 2(2010), No. 1, art. No. 18.

[14] F. Hassani, P.M. Nekoovaght, and N. Gharib, The influence of microwave irradiation on rocks for microwave-assisted underground excavation, *J. Rock Mech. Geotech. Eng.*, 8(2016), No. 1, p. 1.

[15] M. Nicco, E.A. Holley, P. Hartlieb, R. Kaunda, and P.P. Nelson, Methods for characterizing cracks induced in rock, *Rock Mech. Rock Eng.*, 51(2018), No. 7, p. 2075.

[16] D.A. Jones, S.W. Kingman, D.N. Whittles, and I.S. Lowndes, Understanding microwave assisted breakage, *Miner. Eng.*, 18(2005), No. 7, p. 659.

[17] R. Meisels, M. Toifl, P. Hartlieb, F. Kuchar, and T. Antretter, Microwave propagation and absorption and its thermo-mechanical consequences in heterogeneous rocks, *Int. J. Miner. Process.*, 135(2015), p. 40.

[18] T.T. Chen, J.E. Dutrizac, K.E. Haque, W. Wyslouzil, and S. Kashyap, The relative transparency of minerals to microwave radiation, *Can. Metall. Q.*, 23(1984), No. 3, p. 349.

[19] G.M. Lu, Y.H. Li, F. Hassani, and X.W. Zhang, The influence of microwave irradiation on thermal properties of main rock-forming minerals, *Appl. Therm. Eng.*, 112(2017), p. 1523.

[20] Y.L. Zheng, X.B. Zhao, Q.H. Zhao, J.C. Li, and Q.B. Zhang, Dielectric properties of hard rock minerals and implications for microwave-assisted rock fracturing, *Geomech. Geophys. Geo Energy Geo Resour.*, 6(2020), No. 1, art. No. 22.

[21] G.M. Lu, X.T. Feng, Y.H. Li, F. Hassani, and X.W. Zhang, Experimental investigation on the effects of microwave treatment on basalt heating, mechanical strength, and fragmentation, *Rock Mech. Rock Eng.*, 52(2019), No. 8, p. 2535.

[22] M. Nicco, E.A. Holley, P. Hartlieb, and K. Pfaff, Textural and mineralogical controls on microwave-induced cracking in granites, *Rock Mech. Rock Eng.*, 53(2020), No. 10, p. 4745.

[23] H. Li, S.L. Shi, B.Q. Lin, *et al.*, A fully coupled electromagnetic, heat transfer and multiphase porous media model for microwave heating of coal, *Fuel Process. Technol.*, 189(2019), p. 49.

[24] B.Q. Lin, H. Li, Z.W. Chen, C.S. Zheng, Y.D. Hong, and Z. Wang, Sensitivity analysis on the microwave heating of coal: A coupled electromagnetic and heat transfer model, *Appl. Therm.*

Eng., 126(2017), p. 949.

[25] S. Li, Y.M. Zhang, Y.Z. Yuan, and P.C. Hu, An insight on the mechanism of efficient leaching of vanadium from vanadium shale induced by microwave-generated hot spots, *Int. J. Miner. Metall. Mater.*, 30(2023), No. 2, p. 293.

[26] T. Xu, Y. Yuan, M.J. Heap, G.L. Zhou, M.S.A. Perera, and P.G. Ranjith, Microwave-assisted damage and fracturing of hard rocks and its implications for effective mineral resources recovery, *Miner. Eng.*, 160(2021), art. No. 106663.

[27] P. Nekoovaght, N. Gharib and F. Hassani, Numerical simulation and experimental investigation of the influence of 2.45 GHz microwave radiation on hard rock surface, [in] *Proceedings of the ISRM International Symposium-8th Asian Rock Mechanics Symposium*, Sapporo, Japan, 2014.

[28] M. Pressacco, J.J.J. Kangas, and T. Saksala, Numerical modelling of microwave heating assisted rock fracture, *Rock Mech. Rock Eng.*, 55(2022), No. 2, p. 481.

[29] Y.L. Zheng and T.W. Sun, A method to derive the dielectric loss factor of minerals from microwave heating rate tests, *Measurement*, 171(2021), art. No. 108788.

[30] G.L. Cui, T.Y. Chen, X.T. Feng, *et al.* , Coupled multiscale-modeling of microwave-heating-induced fracturing in shales, *Int. J. Rock Mech. Min. Sci.*, 136(2020), art. No. 104520.

[31] J.L. Li, R.B. Kaunda, S. Arora, P. Hartlieb, and P.P. Nelson, Fully-coupled simulations of thermally-induced cracking in pegmatite due to microwave irradiation, *J. Rock Mech. Geotech. Eng.*, 11(2019), No. 2, p. 242.

[32] Q.H. Zhao, X.B. Zhao, Y.L. Zheng, J.C. Li, L. He, and C.J. Zou, Microwave fracturing of water-bearing sandstones: Heating characteristics and bursting, *Int. J. Rock Mech. Min. Sci.*, 136(2020), art. No. 104495.

[33] J. Trčková, R. Živor, and R. Přikryl, Physical and mechanical properties of selected amphibolite core samples from the Kola Superdeep Borehole KSDB-3, *Terra Nova.*, 14(2002), No. 5, p. 379.

[34] H. Li, C.S. Zheng, J.X. Lu, *et al.*, Drying kinetics of coal under microwave irradiation based on a coupled electromagnetic, heat transfer and multiphase porous media model, *Fuel*, 256(2019), art. No. 115966.

[35] D.Y. Li, X.L. Su, F.H. Gao, and Z.D. Liu, Experimental studies on physical and mechanical behaviors of heated rocks with prefabricated hole exposed to different cooling rates, *Geomech. Geophys. Geo Energy Geo Resour.*, 8(2022), No. 4, art. No. 125.

[36] J.S. Zeng, Q.J. Hu, Y. Chen, *et al.*, Experimental investigation on structural evolution of granite at high temperature induced by microwave irradiation, *Mineral. Petrol.*, 113(2019), No. 6, p. 745.

[37] N. Doungkaew and P. Eichhubl, High-temperature fracture growth by constrained sintering of jadeite and quartz aggregates, *J. Geophys. Res. Solid Earth*, 128(2023), No. 4, art. No. e2022JB025565.

[38] J.X. Huang, G. Xu, Y.P. Liang, G.Z. Hu, and P. Chang, Improving coal permeability using microwave heating technology—A review, *Fuel*, 266(2020), art. No. 117022.

[39] A. Acosta-Vigil, D. London, and G.B. Morgan, Experiments on the kinetics of partial melting of a leucogranite at 200 MPa H_2O and 690–800°C: Compositional variability of melts during the onset of H_2O-saturated crustal anatexis, *Contrib. Mineral. Petrol.*, 151(2006), No. 5, p. 539.

[40] J.A. Grant, Liquid compositions from low-pressure experimental melting of pelitic rock from Morton Pass, Wyoming, USA, *J. Metamorph. Geol.*, 22(2004), No. 2, p. 65.

[41] S.K. Roy, D. Nayak, N. Dash, N. Dhawan, and S.S. Rath, Microwave-assisted reduction roasting—Magnetic separation studies of two mineralogically different low-grade iron ores, *Int. J. Miner. Metall. Mater.*, 27(2020), No. 11, p. 1449.